scientific reports

Check for updates

OPEN

Using optical absorption to reduce cross-talk in spatially multiplexed waveguiding metasurfaces

Samuel Loke[1,2], Zhengli Wu[1], Emmanuel Lassalle[1,2]✉ & Ramon Paniagua-Dominguez[1,2]✉

Dual-wavelength metasurfaces often employ spatial multiplexing design concepts where two interleaved lattices of meta-atoms, each designed for a specific wavelength, occupy the same layer. However, this arrangement incurs efficiency losses as each wavelength inevitably "sees" unintended meta-atoms designed for the other wavelength, causing spurious interference (crosstalk) effects, which are especially affecting the shorter wavelength. In this paper, we numerically demonstrate that the crosstalk can be reduced by introducing some optical absorption at the shorter wavelength, unveiling the near-field mechanisms at play. Then, through designing and simulating a dual-wavelength beam-steering metasurface, we demonstrate the benefits of certain level of absorption in terms of wavefront purity (characterized by the diffraction efficiency into a desired blazed order) and beam-steering efficiency. This method also presents some advantages in its simplicity as it allows to use the traditional phase-mapping approach based on the simulations of two independent meta-atom libraries, compared to more complex methods that require accounting for the crosstalk between meta-atoms.

Optical metasurfaces offer an exciting avenue for realizing advanced and novel optical applications[1]. By scattering light using subwavelength-spaced nanostructures, metasurfaces can modulate the properties of light fields, such as their phase, amplitude and polarization. This enables powerful control over light propagation just from wavefront engineering alone, and indeed, beam-steering metasurfaces and metalenses are amongst the forefront of optical metasurface applications[2,3].

Due, however, to their strong chromatic dispersion, most of the beam-steering metasurfaces and metalenses are monochromatic (i.e. are designed to operate at a single wavelength), and their design has traditionally and successfully relied upon the *phase-mapping approach*, which assumes that a phase-delay is *locally* imparted on the incident light, i.e. at the level of each individual nanostructure (called "meta-atoms"), which are typically arranged in a subwavelength lattice to avoid undesirable diffraction. For this approach to be valid, the optical near-field interactions (also referred to as "crosstalk") between nanostructures must be negligible so that the behavior of a single nanostructure is mostly independent from its neighbors. This can be realized using high-index dielectric nanostructures and operating at a certain duty cycle[2], which helps to strongly confine the light within the nanostructure[2,4,5]. One can then build a library of meta-atoms imparting various phase-delays to directly map a desired phase profile, based on the simulation of unit-cells, usually relying on the local periodic approximation (i.e. on the assumption that the metasurface is *locally* similar to a periodic array of meta-atoms).

One way to extend the functionality of a metasurface to two wavelengths (or more) is through spatial multiplexing[6–10], which consists in encoding two (or more) independent phase profiles using different sets of nanostructures[2]. One of the method of spatial multiplexing is meta-atom interleaving[8], where the two phase profiles are encoded using two interleaved lattices that occupy the same layer.

However, while the phase-mapping approach works very well at one wavelength (except perhaps at very large bending angles[11,12]), using this approach for two wavelengths in the interleaving method present some difficulties. Indeed, in order to remain in the sub-diffraction regime, the following condition must be respected: the *shorter* wavelength should be larger than the Rayleigh wavelength, defined as (in the case of hexagonal lattice):

[1]Institute of Materials Research and Engineering (IMRE) Agency for Science, Technology and Research (A*STAR) , 2 Fusionopolis Way, Innovis #08-03, 138634 Singapore, Republic of Singapore. [2]National Semiconductor Translation and Innovation Centre (NSTIC), 1 Fusionopolis Way, #19-10 Connexis North, 138632 Singapore, Republic of Singapore. ✉email: emmanuel_lassalle@imre.a-star.edu.sg; ramon_paniagua@imre.astar.edu.sg

$$\lambda_R = \frac{n_s\sqrt{3}}{2}p$$

with n_s the refractive index of the substrate on which the meta-atoms are standing, and p the lattice constant of the lattice encoding the *longer* wavelength phase profile. Otherwise, a significant portion of the light is lost into undesired diffraction orders. For this condition to be met, the meta-atoms must be closely packed, which in turn can create non-negligible crosstalk. While crosstalk can usually be neglected for the longer wavelength (because the nanostructures encoding the phase profile for the short wavelength will in general be optically small for the long wavelength), this is usually not true for the short wavelength. Hence, for the short wavelength, the traditional phase-mapping approach breaks down, resulting in low efficiencies for the metasurface performance and creation of spurious focal spots[8]. Efforts have been made to extend the phase-mapping approach by taking into account the crosstalk between nearby meta-atoms in dual-wavelength metalenses, giving rise to the concept of "meta-molecules"[13], but rely on more complex simulations of meta-molecule library. Adjoint optimization and machine learning assisted inverse design methods have been applied to design numerous broadband and multiwavelength metasurfaces[14–16] but are also much more computationally demanding. Finally, bilayer metasurfaces have also been used to design achromatic or multi-wavelength metasurfaces, relying on the extra degrees of freedom[17–19]. While a powerful design, multilayer metasurfaces increase design and fabrication complexity. As such there is value in focusing on single layer, multiplexed metasurfaces.

In this work, we show that the validity of the traditional phase-mapping approach can be restored in a meta-atom interleaving method provided that some level of optical absorption exists at the shorter wavelength. To illustrate this, we consider a dual-wavelength metasurface working in transmission that employs nanopillars with circular cross-sections, arranged in two interleaved lattices. We first use full-wave simulations of a dual-wavelength metasurface working at 900 nm and 620 nm to investigate how the presence of absorption helps to mitigate the near-field coupling at the shortest wavelength. We evidence the effect of optical absorption on the crosstalk by looking at the field confined within the meta-atoms, showing that absorption restores local interactions with light. Then, we study a dual-wavelength beam-steering metasurface to show that absorption helps to improve the purity of the wavefront steered into the desire (blazed) order, in turn reducing the amount of power into spurious diffraction orders. Not surprisingly, the presence of absorption also decreases the overall transmission, but we show that this trade-off between "purity of the wavefront" and "low transmission" can result in an ideal absorption level that maximizes the absolute diffraction efficiency into the blazed order.

Combined with existing available methods to experimentally tune the absorption of materials (via, e.g., hydrogenating amorphous silicon[20]), these findings suggest that *absorption engineering* can help to optimize the performances of metasurfaces spatially multiplexed via interleaving meta-atoms, without having to rely on complex and computationally demanding designs.

Results

To realize a dual-wavelength metasurface, we employ a spatial multiplexing technique which consists of interleaving two sets of nanopillars onto a shared lattice, where each set of pillars is meant to manipulate either the 900 nm or the 620 nm wavelength. Figure 1a-c show the schematics of the unit-cell of such a lattice. The 900 nm nanopillars (labelled by A in Fig. 1b) are arranged in a hexagonal lattice with lattice constant $p = 460$ nm, and the 620 nm nanopillars (labelled by B in Fig. 1b) are arranged in a hexagonal lattice with lattice constant $p\prime = p/2 = 230$ nm, filling the positions unoccupied by the type A nanopillars. The nanopillars stand on a glass substrate of refractive index $n_s = 1.46$ and are encapsulated in a polymer matrix of refractive index $n_m = 1.59$ (see Fig. 1c). The pillars have a height of h=500 nm and the polymer matrix has a thickness of 550 nm (i.e. covering the pillars with an extra 50 nm on top, see Fig. 1c). The polymer encapsulation is not necessary for this study, but is preferable in certain cases to protect the nanopillars, such as in vivo applications (e.g[21]). Keeping such applications in mind, we also consider the medium on top of the metasurface to be water (refractive index $n_w = 1.33$, see Fig. 1c). For the nanopillar material, we use amorphous silicon (aSi) whose optical constants are: at 620 nm, refractive index $n_{620} = 4.38$ and extinction coefficient $k_{620} = 0.14$; and at 900 nm, $n_{900} = 3.83$, and $k_{900} = 0$ (negligible losses).

We start by performing Rigorous Coupled Wave Analysis (RCWA)[22–25]using the RETICOLO code[26], on the rectangular unit-cell of periodicity $p = 460$ nm by $p\sqrt{3} = 797$ nm (shown in Fig. 1b). Normally incident plane waves coming from the substrate side and linearly polarized along the y-axis (electric field component E_y with amplitude equal to unity) were used with wavelength 900 nm and 620 nm. The choice of polarization along the y-axis is arbitrary, and the other polarization along x-axis would lead to similar results. In each simulation, we sweep the diameters of the A and B nanopillars, D_A and D_B, respectively, and record the phase-delay accumulated after propagation through the metasurface and onto the transmission medium, which we assume to be water, as mentioned previously. The A nanopillar diameters vary from 60 nm to 250 nm, and the B nanopillar diameters vary from 40 nm to 130 nm. These ranges of diameters are chosen to form a library that spans the entire phase space from 0 to 2π for each wavelength. Figure 1d shows the phase map for the 900 nm wavelength, for which aSi presents no absorption ($k_{900} = 0$). One can see that the phase varies steadily with D_A to achieve a smooth 0-to-2π phase coverage, largely not affected by D_B. This is an almost ideal case of minimal crosstalk between A and B nanopillars, because the nanopillars B are optically small compared to the 900 nm wavelength, and therefore do not interact significantly with the 900 nm wavelength, almost not altering the phase[8].

To evidence the role of absorption at the 620 nm wavelength, we first simulate the phase map in Fig. 1e under no absorption assumption (setting $k_{620} = 0$). The crosstalk between A nanopillars and B nanopillars at 620 nm is evident and results in abrupt phase variations across the D_A range, causing "noise" in the phase map

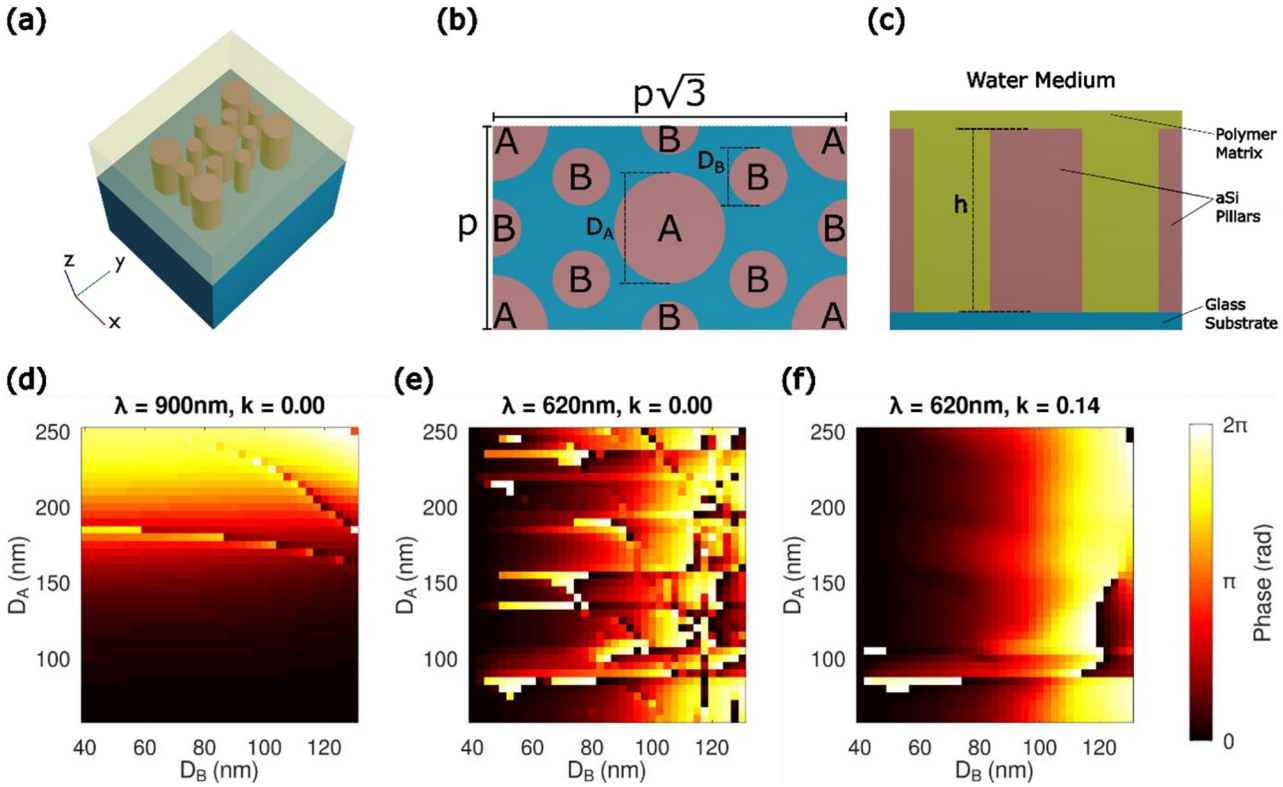

Fig. 1. Phase-mapping approach applied to a spatially multiplexed (meta-atom interleaving) dual-wavelength metasurface. (**a**) 3D, (**b**) top and (**c**) vertical cross-section (along x-axis) views of a single unit-cell. (**d**-**f**) Phase maps of the periodic arrangement of these unit-cells with varying nanopillar diameters D_A and D_B, (**d**) at 900 nm under no absorption ($k_{900} = 0$), (**e**) at 620 nm under no absorption ($k_{620} = 0$) and (**f**) at 620 nm with absorption ($k_{620} = 0.14$). The "0 phase reference" is chosen with respect to the smallest nanopillars case, i.e. D_A = 60 nm and D_B = 40 nm.

and resulting in an unpredictable mapping of the phase with D_B (as it highly depends on $D_A$too). This is because, at this wavelength, the A nanopillars are optically large and their interaction with the 620 nm light is important, drastically altering the phase[8].

This situation changes as soon as some absorption is present in the pillars (when $k_{620} = 0.14$): the noise is "suppressed", as seen in Fig. 1f, and an almost "ideal" phase map is restored for 620 nm, where the phase varies steadily with D_B to achieve a smooth 0-to-2π phase coverage, largely unaffected by D_A. As it becomes apparent, the phase map displays minimal crosstalk between the two types of waveguide channels, as propagation through the type A pillars is suppressed in the presence of material absorption, leading to low D_A dependance. Note that absorption should in principle suppress propagation through both A and B pillars, however, it suppresses propagation through A pillars more so than B pillars because of their larger sizes (which leads to higher field confinement and thus, higher absorption). Obviously, while the phase map looks better, this comes at the cost of an overall decrease in transmission (as seen in Figure S1 of the Supplementary Information). However, as we will eventually see, even with this decrease in transmission, the presence of absorption can still help to increase the overall metasurface efficiency.

To develop a clearer picture of how absorption affects crosstalk at 620 nm, we investigate in Fig. 2 the magnetic field intensity distribution inside the type B nanopillars for three different cases, displayed in Table 1. These cases were chosen such that: in Case I, both A and B pillars are at the smallest diameter of their respective libraries; in Case II, D_A is smallest while D_B is largest of their respective libraries; and in Case III, D_A and D_B are the largest of their respective libraries. These near fields were calculated with RETICOLO RCWA.

In Fig. 2a-c, we show the near-field distributions across the pillars (specifically, the absolute amplitude of the magnetic field component $|H_x|$) at 620 nm (with $k_{620} = 0.14$) in each unit-cell associated to the Cases I, II and III, respectively. Their equivalents for the non-absorption case ($k_{620} = 0$) are plotted in Figure S2 of the Supplementary Information. We integrate these fields along the vertical z-axis to average the variations across the z-axis. One can see that in all cases the magnetic field intensity is mostly confined within the nanopillars (cross-sections delimited by white circles). In Cases I and II, the larger nanopillars confine light more than the smaller ones, i.e. type A nanopillars in Case I (Fig. 2a), and type B nanopillars in Case II (Fig. 2b). However, in Case III (Fig. 2c), this is not the case, and light is more confined within certain (but not all) type B nanopillars, which are smaller than A nanopillars. The reason why the light confinement is not the same within identical pillars is because the H_x component of light – or equivalently the E_y component of the electric field - experiences different surrounding environments in terms of neighbouring nanopillars, as will be seen later. This is evidence

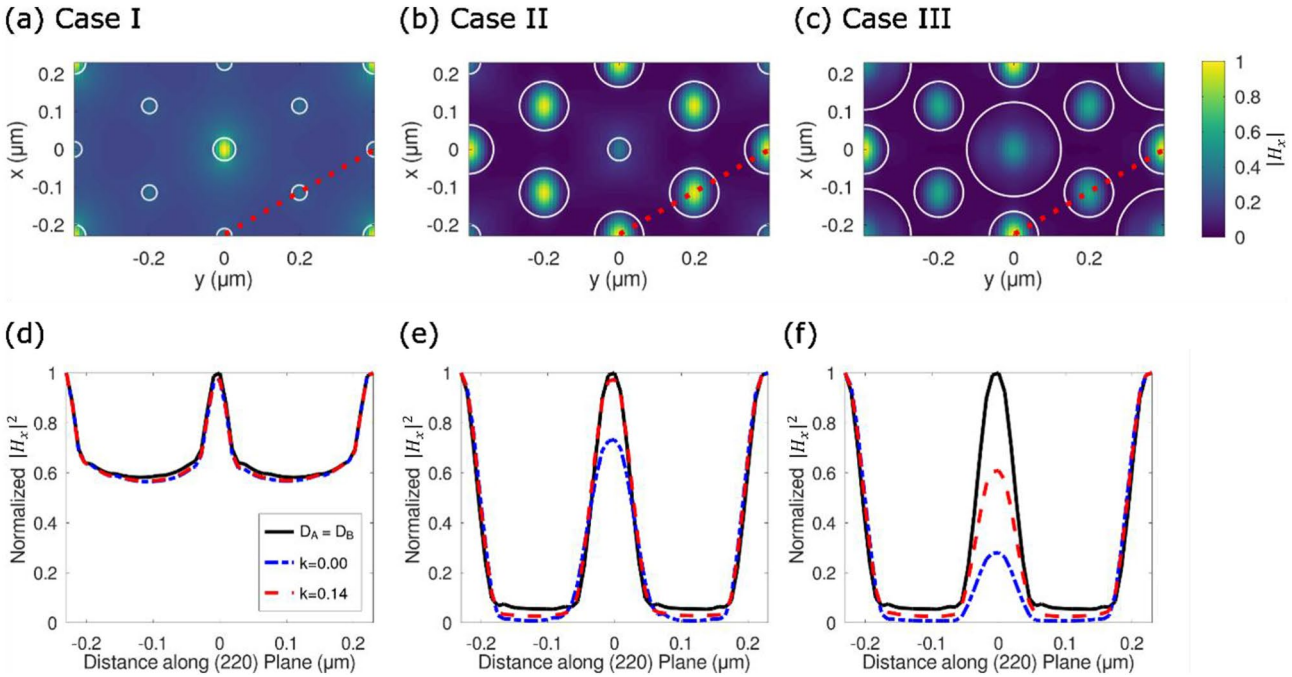

Fig. 2. Magnetic field distributions at the 620 nm wavelength, integrated across the vertical z-axis of the unit-cells. (a), (b) and (c) plot the absolute amplitude of the magnetic field component $|H_x|$ at 620 nm, $k_{620} = 0.14$, for cases I, II and III respectively. The red dotted lines in these figures are the plane used in the plots (d), (e) and (f), which plot the relative magnetic intensity (proportional to $|H_x|^2$ and normalized to the highest value in each scenario) of the respective cases for three different scenarios: no absorption $k_{620} = 0$ (blue lines), absorption $k_{620} = 0.14$ (red lines) and ideal scenario $k_{620}=0.14$ and $D_A = D_B$ (black lines).

Case	D_A (nm)	D_B (nm)
I	60	40
II	60	130
III	250	130

Table 1. Nanopillar dimensions for the three cases examined in Fig. 2.

of the interplay between light confinement and absorption: the larger the nanopillars, the more they can confine the light, but also the more they absorb the light, reducing the amount of light energy within the pillars.

In order to show the near-fields behavior with and without absorption, we then take a diagonal cut in the x-y plane with Miller indices (220) (indicated by the red dotted lines in Fig. 2a-c), and plot in Fig. 2d-f the relative magnetic intensity distribution proportional to $|H_x|^2$ (intensity normalized by the highest value in each scenario) in the different scenarios: under no absorption $k_{620} = 0$ (blue dashed lines) and with absorption $k_{620} = 0.14$ (red dashed lines). Each line in each plot is normalized against their individual maxima. This allows us to visualize the distribution of fields in the type B nanopillars, which encode the phase for the 620 nm wavelength. Finally, we also plot for reference the case where type A nanopillars are absent and replaced by type B nanopillars, which is the "ideal" scenario where no crosstalk between A nanopillars and B nanopillars is present, i.e. $k_{620}=0.14$ and $D_A = D_B$ (black plain lines). Importantly, one can see that in the ideal scenario, the intensity distribution is identical within each nanopillar, leading to a well-defined phase that is directly related to the nanopillar diameter. Thus, one can use a direct one-to-one mapping between phase and nanopillar diameter, which is the principle of the local phase-mapping approach.

One can see that in the Case I (Fig. 2d), the relative magnetic intensity distribution remains unchanged with ($k_{620}=0.14$) or without ($k_{620}=0$) absorption, and very similar to the ideal case ($D_A = D_B$). This is because the nanopillars are too small in this case to lead to significant crosstalk. However, the situation changes in Case II (Fig. 2e). Without absorption ($k_{620}=0$), the relative magnetic intensity distribution is not the same anymore in all the nanopillars. While the nanopillars at the bottom and top of the diagonal have same intensity distribution, the nanopillar in the center of the diagonal has a different (lower) intensity. This is evidence of crosstalk, as the incident light linearly polarized along y axis will see the same surrounding environment (i.e. neighboring nanopillars) for the first two nanopillars but will see a different surrounding environment for the central nanopillar. This leads to a phase that is not well-defined, as it depends not only on the diameter of the B nanopillars but also on their surrounding nanopillars. The ideal relative intensity distribution can be almost

fully restored by the presence of absorption ($k_{620}=0.14$), shedding light on the mechanisms that transform the "noisy" phase map of Fig. 1e into the "smooth" phase map of Fig. 1f. Finally, in the Case III (Fig. 2f), the presence of absorption helps to only partially restore an ideal relative intensity distribution compared to the non-absorption scenario. This is because the A nanopillars are the largest out of the three cases, resulting in even more crosstalk.

This idea, where absorption can lead to competing phenomena between reduced transmission and improved wavefront mapping via reduced crosstalk, can be further investigated. To do so, we design a beam-steering metasurface (also called "phase-gradient metasurface"[27]) consisting of a periodic array of super-cells made of interleaved nanopillars, such that the metasurface deflects the $\lambda=900$ nm and $\lambda=620$ nm incident light (coming at normal incidence with electric field polarization along the super-cell width) into the same blazed angle (see Fig. 3a). Such a metasurface is a good approximation of one of the Fresnel zones of a dual-wavelength metalens focusing to the same focal distance, which locally looks like a phase-gradient metasurface bending the two wavelengths into the same direction.

To design such a dual-wavelength metasurface, one must find the phase profile ϕ_i encoded by each sub-lattice that will lead to the same deflected angle θ_t, called the blazed angle $\theta_t = \theta_{Blazed}$. For a metasurface working in transmission, the generalized Snell's law reads (for normally incident light)[28]:

$$n_t \sin\theta_t = \frac{\lambda_i}{2\pi}\frac{\partial\phi_i}{\partial r} \tag{1}$$

where n_t is the refractive index of the medium where the light is transmitted (in our case water, $n_t = n_w = 1.33$), λ_i is the wavelength of incident light in vacuum, ϕ_i is the phase imparted by the metasurface for wavelength λ_i, and r denotes the position on the metasurface. For a beam-steering metasurface, the phase-gradient is constant and reads: $\frac{\partial\phi}{\partial r} = m_i 2\pi/\mathrm{d}$, where m_i is the blazed diffraction order (integer) and d is the supercell length (same phase profile as for a blazed grating[29]). One can see that to have same blazed angle θ_{Blazed} at both wavelengths, one must satisfy the condition: $m_{620}\lambda_{620} = m_{900}\lambda_{900}$ with m_i being integers. Since $\lambda_{900} \simeq \frac{3}{2}\lambda_{620}$, this approximately amounts to satisfy the condition: $\frac{m_{620}}{m_{900}} = \frac{3}{2}$.

Therefore, in the example that we will study hereafter, we choose to encode the following phase profiles: $\frac{\partial\phi_i}{\partial r} = m_i 2\pi/\mathrm{d}$ with $m_{620}=3$ and $m_{900}=2$ and $\mathrm{d}=18\mathrm{p}=8.28\,\mu\mathrm{m}$. This leads to approximately the same bending angle about $\theta_{Blazed} \simeq 10°$ (more exactly, at 900 nm $\theta_{Blazed}=9.4°$, and at 620 nm $\theta_{Blazed}=9.8°$, according to Eq. (1)). Note that the period d is chosen here to contain exactly 2 periods $\mathrm{d}_{900}=9p$ and 3 periods $\mathrm{d}_{620}=6p$, each sampling the phase from 0 to 2π for 900 nm and 620 nm wavelengths, respectively (see Fig. 3b). The total super-cell length is $\mathrm{d}=18\mathrm{p}=8.28\,\mu\mathrm{m}$ and the width is $p\sqrt{3}$. To map the phase profile, we choose the nanopillars radii from the libraries simulated in Fig. 1d and f, which are almost identical as two independent meta-atom libraries (simulated without the nanopillars encoding the other wavelength).

We then conduct a diffraction analysis of this metasurface based on the Finite-Difference Time-Domain (FDTD) method, using Ansys Lumerical software. We again use a linear polarization along y-axis, but the results for a x-polarization are expected to be similar (see for example Table S1 of Supplementary Information in Ref.[30]). First of all, we find that, as expected, most of the energy is deflected into the angles 9.3° and 9.7° for $\lambda=900$ nm and $\lambda=620$ nm, respectively (not shown here), in good agreement with the aforementioned angles calculated from Eq. (1), revealing that the multiplexed dual-wavelength metasurface is qualitatively working as intended. To be more quantitative, Fig. 3c-e show the Diffraction Efficiency in the first 6 diffraction orders at 900 nm and 620 nm ($m_i = 0, \ldots, 5$), defined as the energy inside the diffraction order m_i normalized by the transmitted energy, i.e., as the fraction of transmitted light that transmits into a given diffraction order. Summing up all diffraction efficiencies will yield an efficiency of 100%. For 900 nm light (Fig. 3c), we can see that most of the energy is channeled into the diffraction order $m_{900}=2$, as expected, with a relatively high Diffraction Efficiency of 66.8%. We then compared in Fig. 3d and e the case at 620 nm without ($k=0$, Fig. 3d) and with absorption ($k=0.14$, Fig. 3e). Note that for Fig. 3d, the pillar radii are chosen based on the phase map in Fig. 1f, with k deliberately set to 0. In both cases most of the energy is channeled into the diffraction order $m_{620}=3$, as expected. Importantly, one can see that the presence of absorption helps to restore a Diffraction Efficiency similar (even better) than the 900 nm wavelength, i.e. 72.0% Diffraction Efficiency with absorption compared to 45.9% Diffraction Efficiency without absorption. This is sheer evidence that absorption helps to purify the wavefront by suppressing the crosstalk, thus reducing the amount of energy into the undesired diffraction channels, and increasing it into the desired channel (the blazed order) relative to the other ones.

This analysis, however, does not account for the reduction of the transmission incurred by the presence of absorption for the 620 nm light. The final fraction of the incident light going into the desired diffraction order is affected by both diffraction efficiency and transmission, and both must be accounted for to achieve an optimum performance. In order to quantify the relationship and potential tradeoff between these two factors, we also need to look at the total Transmission in the system. In Fig. 3f, we compute both the Diffraction Efficiency into the blazed order and the total Transmission at $\lambda=620$ nm as a function of the extinction coefficient k, which we allow to vary from $k=0$ to $k=0.14$, while keeping the same nanopillar arrangement. Keeping the same geometry allows us to evidence directly the effect of absorption on the crosstalk.

Tuning the extinction coefficient can be done in practice, using hydrogenated amorphous Silicon (aSi:H), whose real (n) and imaginary (k) refractive indices can be tuned by controlling the hydrogenation and silicon disorder through adjusting the chemical deposition conditions[20]. For this numerical study, we thus assume an ideal scenario where, at 620 nm, k_{620} is tunable between 0.00 and 0.14 while n_{620} remains constant at 4.38 (note that in practice n will also slightly change, but this change can always be taken into account by adjusting the nanopillar diameters in the meta-atom library).

The Total Efficiency at 620 nm is defined as follows:

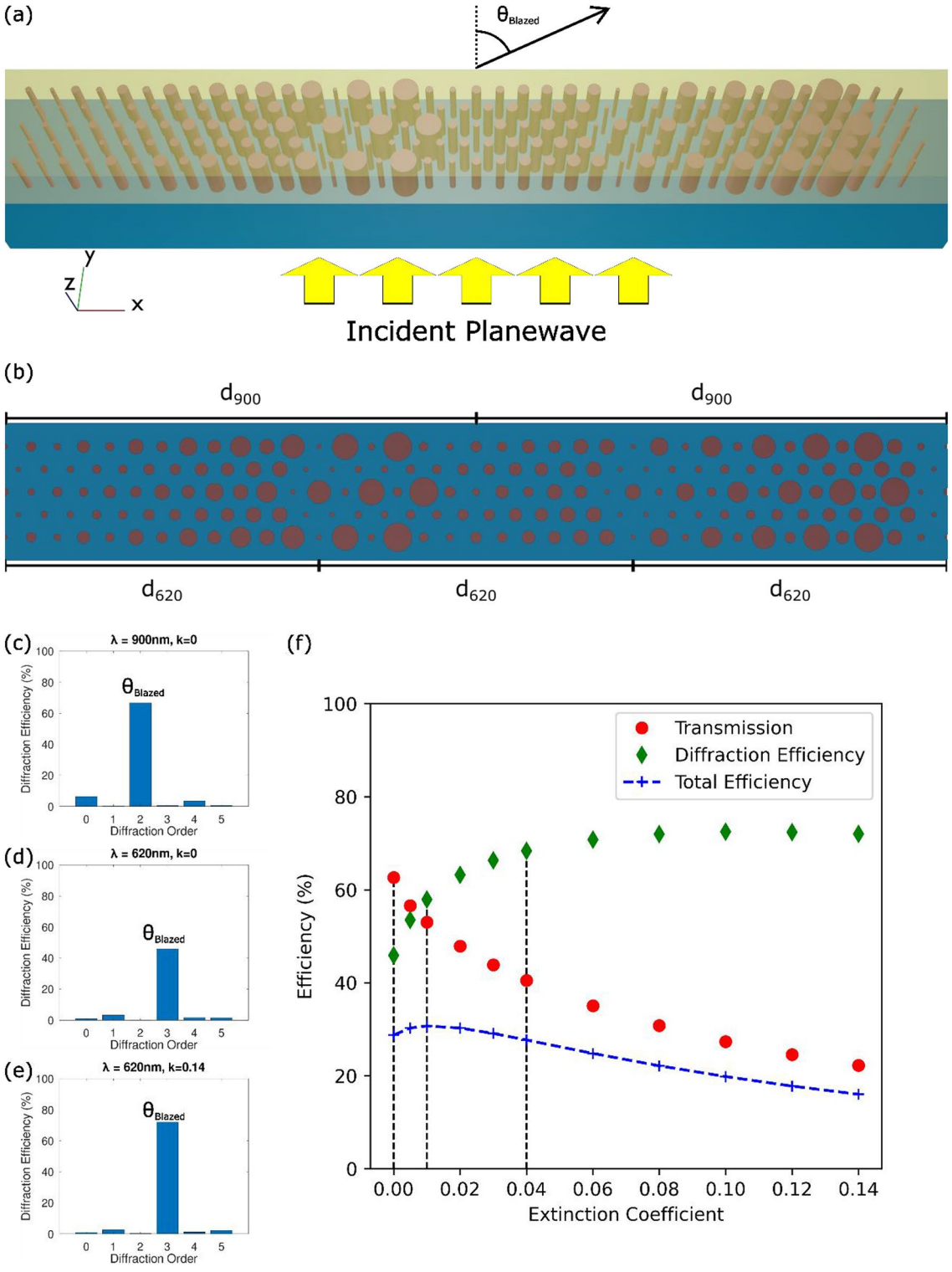

Fig. 3. Simulated diffraction from a dual-wavelength beam-steering metasurface. Schematics of the supercell of this diffraction grating are shown in (a) perspective view and (b) orthographic projection. Diffraction efficiency (normalized with respect to the total transmitted light) of the first 5 diffraction orders are plotted for (c) $\lambda = 900$ nm, $k = 0$, (d) $\lambda = 620$ nm, $k = 0$ and (e) $\lambda = 620$ nm, $k = 0.14$. (f) Transmission, diffraction and total beam-steering efficiencies at $\lambda = 620$ nm of the third diffraction order as a function of the extinction coefficient of the nanopillars' material.

$$\text{Total Efficiency} = \text{Transmission} \times \text{Diffraction Efficiency} \quad (2)$$

which defines the overall metasurface or beam-steering efficiency (i.e. the percentage of energy of the incident light that is channeled into the blazed order).

Figure 3f plots these three figures-of-merit. One can see that, as extinction coefficient k increases, the Transmission decreases monotonically. This is expected as the presence of absorption reduces the portion of transmitted light. Interestingly, even for $k = 0$, the Transmission is not equal to 100%, reaching values only slightly above 60%. This comes from the fact that the lattice constant p is not deeply sub-wavelength for the shorter wavelength $\lambda = 620$ nm, which is close enough to the Rayleigh wavelength $\lambda_R = \frac{n_s\sqrt{3}}{2}p \simeq 582$ nm to allow multiple higher diffraction orders to be excited in reflection (inside the substrate) when the super-cell is considered[8,13]. We also highlight here that the use of a square lattice would not be a good choice here, as the Rayleigh wavelength λ_R would read in that case: $\lambda_R = n_s p \simeq 672$ nm, making shorter wavelength diffractive even at the unit-cell level, and thus leading to even higher power channeling into unwanted reflected diffraction orders.

Noteworthy, at the same time, the Diffraction Efficiency increases and "plateaus" at $\simeq 72\%$ after $k = 0.08$. The increase is because, as we have seen above, the absorption reduces the crosstalk, thus leading to cleaner wavefront and, in turn, improving the relative diffraction efficiency. It is interesting to note that after a certain value ($k = 0.08$ here), there is no benefit in increasing the absorption further, indicating that cross-talk has been fully suppressed for that k value.

The competition between these two figures-of-merit lead to a non-intuitive behavior for the Total Efficiency, which first increases before decreasing with k, showing a maximum at around $k = 0.01$ (highlighted by a vertical black dashed line). Also, after $k > 0.01$ the Total Efficiency decreases monotonically but at a slower rate than the Transmission Efficiency, due to the interplay between Diffraction Efficiency and Transmission Efficiency. Therefore, keeping in mind that, as k increases the Diffraction Efficiency increases, these results seem to indicate that some level of absorption might be beneficial in this type of configuration. For example, at $k = 0.04$, where the Total Efficiency is about the same as the case without absorption - that is about 30% - the Diffraction Efficiency is increased from about 46% to 68% (highlighted by vertical black dashed lines). This represents an important improvement of the *purity* of the emerging wavefront from the metasurface, leading to the power being channeled mainly to the desired order, and removing spurious channels that could result, e.g. into background noise or higher order foci in a metalens (like in Ref.[8]). All these observations suggest that from an engineering perspective, there is some performance optimization to be gained from engineering the extinction coefficient of the nanopillars in interleaved metasurfaces, as to mitigate the crosstalk and improve wavefront purity and/or total efficiency. Similar observations are made for different super-cells, i.e. for different blazed orders (as seen in Figure S3 of the Supplementary Information).

Discussion

Using full-wave simulations, we have shown how material absorption can help to mitigate the crosstalk between nanopillars in dual-wavelength metasurfaces spatially multiplexed through the interleaving method. On one hand, crosstalk at the longer wavelength (900 nm in our case) is typically negligible because the nanopillars operating at the short wavelength (620 nm in our case) are optically small for the longer wavelength. On the other hand, the nanopillars designed to operate at the longer wavelength are typically optically large for the shorter wavelength and induce undesirable crosstalk that cause the failure of the traditional phase-mapping approach. However, by introducing a certain level of absorption at the shorter wavelength, we found that this crosstalk can be mitigated and even almost totally suppressed, albeit at the expense of reducing the total transmission of light. This leads to a trade-off that we highlighted, using as an example the case of a dual-wavelength beam-steering metasurface, between improving the quality of the wavefront emerging from the device (characterized by the diffraction efficiency into the desired blazed angle – or diffraction order), and total efficiency of the device (i.e. the absolute beam-steering efficiency, defined as the portion of energy going into the desire diffraction channel compared to the energy incident on the metasurface). In conclusion, choosing an adequate level of optical absorption in a multiplexed dual-wavelength metasurface to mitigate the crosstalk is crucial to improve the purity and/or total efficiency. This can be achieved with experimental techniques aimed at manipulating the extinction coefficient, like those available during deposition of hydrogenated silicon (aSi: H)[20].

We would also like to comment on the fact that, at the shorter wavelength, the total efficiency is systematically lower than at the longer wavelength for multiplexed metasurfaces using the meta-atom interleaving method, even after reducing the crosstalk drastically. Table 2 below shows a comparison between some literature works and our work (all these numbers are obtained through numerical simulations). It shows that, even with a certain level of absorption, such as the one considered here, one can get similar efficiency levels as those reported in other works that considered negligible losses at the shorter wavelength. For example, using a "meta-molecules" library[13], the authors could drastically reduce the amount of light focused into higher order foci, hence improving the purity of the wavefront, compared to using a standard meta-atom library[8]. However, these efforts have shown little to no improvement of the total focusing efficiency. This is generally attributed to the significant reflections incurred in this, arguably more complex, design, which is also naturally more computationally demanding as it requires generating a larger library of meta-molecules by varying at least two sets of parameters and simulating a larger total area.

As reported previously[8], one reason of the relatively low efficiency (~30%) at the shorter wavelength is the super-periodicity of the metasurface, which induces additional reflection, typically $\sim 20\%$ more, due to the excitation of higher order modes propagating in the substrate. This is a diffraction phenomenon, and it seems difficult to avoid since one cannot decrease the lattice constant too much due to fabrication and material

Reference	Efficiency (at the short wavelength)
[8] (metalens – traditional meta-atom concept)	27%
[13] (metalens – meta-molecule concept)	32%
[13] Supp. Mat. (beam-steering metasurface - – meta-molecule concept)	36% at $\theta_{Blazed} = 5^\circ$ 22% at $\theta_{Blazed} = 20^\circ$
This work (beam-steering metasurface – absorption engineering concept)	30% at $\theta_{Blazed} \simeq 10^\circ$ (value extracted considering $k = 0.01$)

Table 2. Comparison of the total efficiencies for dual-wavelength metasurfaces spatially multiplexed using the meta-atom interleaving method in the literature and this work (all are simulated efficiencies). The efficiencies for metalenses are focusing efficiencies, and for beam-steering metasurfaces it is the total efficiency defined as in Eq. (2). In the literature considered here, the short wavelength is 915 nm and the long wavelength is 1550 nm.

constraints. Perhaps, in the context of metasurface impedance, engineering an additional metasurface to "force" an impedance match could help in reducing this undesirable reflection[31–33].

Also, it should be mentioned that one can increase the total efficiency at the shorter wavelength at the expense of the total efficiency at the longer wavelength for applications where the power needs to be more balanced. This rebalancing can be done for instance by using spatial segmentation[8], i.e. by creating zones in the metasurface where only the lattice for the shorter wavelength is present, instead of the two interleave lattices. Since the nanopillars used for the short wavelength are usually optically small for the long wavelength, this should not induce too much alteration of the wavefront at the long wavelength. This could lead to hybrid designs implementing the two spatial multiplexing methods mentioned in[8].

Overall, the method suggested here to engineer the extinction coefficient of the nanopillars in interleaved dual-wavelength metasurfaces to mitigate the crosstalk and improve wavefront purity and/or total efficiency is attractive in its simplicity, as it allows to keep the use of the usual phase-mapping approach for the two wavelengths independently, resulting in much less simulations compared to other methods which need to take into account the near-field coupling between nanopillars from different lattices (see e.g[13]).

Methods

RCWA simulations were performed using the RETICOLO RCWA code on GNU Octave to calculate phase libraries and near-fields under the local periodic approximation. The incident planewave approaches from a glass substrate background of refractive index $n_s = 1.46$ at normal incidence, propagates through a periodic array of aSi nanopillars of height 500 nm embedded in a polymer layer of index $n_m = 1.59$, and of thickness 550 nm (that is, up to 50 nm above the nanopillars), before exiting into a water medium of index $n_w = 1.33$. Periodic boundary conditions are used with rectangular unit cells of periodicity $p = 460$ nm by $p\sqrt{3} = 797$ nm. These simulations are performed at wavelengths of 620 nm and 900 nm, and at these wavelengths the pillars have refractive indices of $n_{620} = 4.38$ and $n_{900} = 3.83$ respectively. The extinction coefficient (at 620 nm) of these pillars are allowed to vary. The phase delays of the transmitted planewave are calculated as we sweep the pillar diameters, and the near-fields are calculated for select pillar configurations.

FDTD simulations were performed using Ansys Lumerical FDTD to calculate the diffraction response of a blazed grating comprised of several of these unit cells. Using the same set of materials and layers as in the RCWA calculations, a planewave propagates at normal incidence under periodic boundary conditions of $\mathrm{d} = 18\mathrm{p} = 8.28\ \mu\mathrm{m}$ by $p\sqrt{3} = 797$ nm, and the powers going into each diffraction order at 620 nm and 900 nm are computed. Pillar diameters are obtained from the phase maps computed in the RCWA study to map the phase profile given in the main text.

Data availability

The datasets generated during and/or analyzed during the current study are available from the corresponding author on reasonable request.

Received: 27 July 2024; Accepted: 30 September 2024
Published online: 23 October 2024

References

1. Kuznetsov, A. I., Brongersma, M. L., Yao, J., Chen, M. K. & Levy, U. D. P. Tsai, N. I. Zhudelev and e. al., Roadmap for Optical Metasurfaces. *ACS Photonics*, (2024).
2. Lalanne, P. & Chavel, P. Metalenses at visible wavelengths: past, present, perspectives. *Laser Photonics Reviews*. **11** (3), 1600295 (2016).
3. Chen, W. T. & Capasso, F. Will flat optics appear in everyday life anytime soon? *Appl. Phys. Lett.* **118** (10), 100503 (2021).
4. Arbabi, A., Horie, Y., Ball, A. J. & Bagheri, M. Subwavelength-thick lenses with high numerical apertures and large efficiency based on high-contrast transmitarrays. *Nat. Commun.* **6**, 7069 (2015).
5. Khorasaninejad, M. et al. *Polarization-Insensitive Metalenses Visible Wavelengths Nano Letters*, **16**, 11, 7229–7234, (2016).
6. Hu, J., Liu, C. H., Ren, X., Lauhon, L. J. & Odom, T. W. Plasmonic Lattice lenses for Multiwavelength Achromatic focusing. *ACS Nano*. **10** (11), 10275–10282 (2016).
7. Lin, D. et al. Photonic multitasking interleaved Si nanoantenna phased array. *Nano Lett.* **16** (12), 7671–7676 (2016).
8. Arbabi, E., Arbabi, A., Kamali, S. M., Horie, Y. & Faraon, A. Multiwavelength metasurfaces through spatial multiplexing. *Sci. Rep.* **6**, 32803 (2016).

9. Tan, S., Yang, F., Boominathan, V., Veeraraghavan, A. & Naik, G. V. 3D imaging using extreme dispersion in optical metasurfaces. *ACS Photonics*. **8** (5), 1421–1429 (2021).
10. Baek, S. et al. High numerical aperture RGB achromatic metalens in the visible. *Photonics Research*, **10**, 12, pp. B30-B39, (2022).
11. Arbabi, A. et al. Increasing efficiency of high numerical aperture metasurfaces using the grating averaging technique. *Sci. Rep.* **10** (1), 7124 (2020).
12. Paniagua-Domínguez, R. et al. A metalens with a Near-Unity Numerical aperture. *Nano Lett.* **18** (3), 2124–2132 (2018).
13. Arbabi, E., Arbabi, A., Kamali, S. M., Horie, Y. & Faraon, A. Multiwavelength polarization-insensitive lenses based on dielectric metasurfaces with meta-molecules, *Optica*, vol. 3, no. 6, pp. 628–633, (2016).
14. Mansouree, M. et al. Multifunctional 2.5D metastructures enabled by adjoint optimization, *Optica*, vol. 7, no. 1, pp. 77–84, (2020).
15. Li, Z. et al. Meta-optics achieves RGB-achromatic focusing for virtual reality. *Sci. Adv.* **7** (5), eabe4458 (2021).
16. Li, Z. et al. Inverse design enables large-scale high-performance meta-optics reshaping virtual reality. *Nat. Commun.* **13** (1), 1–11 (2022).
17. Zhou, Y. et al. Multilayer noninteracting Dielectric Metasurfaces for Multiwavelength Metaoptics. *Nano Lett.* **18** (12), 7529–7537 (2018).
18. Zhou, Y. et al. Multifunctional metaoptics based on bilayer metasurfaces. *Light: Sci. Appl.* **8** (1), 80 (2019).
19. Kim, J. et al. Photonic encryption platform via Dual-Band Vectorial metaholograms in the Ultraviolet and visible. *ACS Nano*. **16** (3), 3546–3553 (2022).
20. Yang, Y. et al. Revealing Structural Disorder in Hydrogenated Amorphous Silicon for a low-loss Photonic platform at visible frequencies. *Adv. Mater.* **33** (9), 2005893 (2021).
21. Arbabi, E. et al. Two-Photon Microscopy with a Double-Wavelength Metasurface Objective Lens. *Nano Lett.* **18** (8), 4943–4948 (2018).
22. Moharam, M. G., Grann, E. B., Pommet, D. A. & Gaylord, T. K. Formulation for stable and efficient implementation of the rigorous coupled-wave analysis of binary gratings. *JOSA A*. **12** (5), 1068–1076 (1995).
23. Li, L. New formulation of the Fourier modal method for crossed surface-relief gratings, *JOSA A*, pp. 2758–2767, (1997).
24. Lalanne, P. & Jurek, M. P. Computation of the near-field pattern with the coupled-wave method for transverse magnetic polarization. *J. Mod. Opt.* **45** (7), 1357–1374 (1998).
25. Popov, E. & Nevière, M. Grating theory: new equations in Fourier space leading to fast converging results for TM polarization. *JOSA A*. **17** (10), 1773–1784 (2000).
26. Hugonin, J. P. & Lalanne, P. Reticolo software for grating analysis. *Institut d'Optique Plaiseau France*, (2005).
27. Yu, Y. F. et al. High-transmission dielectric metasurface with 2π phase control at visible wavelengths. *Laser Photonics Reviews*. **9** (4), 412–418 (2015).
28. Yu, N. et al. Light propagation with phase discontinuities: generalized laws of reflection and refraction. *Science*. **334** (6054), 333–337 (2011).
29. Bonod, N. & Neauport, J. Diffraction gratings: from principles to applications in high-intensity lasers. *Adv. Opt. Photonics*. **8** (1), 156–199 (2016).
30. Lassalle, E. et al. Imaging properties of large field-of-view quadratic metalenses and their applications to Fingerprint Detection. *ACS Photonics*. **8** (5), 1457–1468 (2021).
31. Ra'Di, Y., Asadchy, V. S. & Treyakov, S. A. Total absorption of electromagnetic waves in ultimately thin layers. *IEEE Trans. Antennas Propagation*, **61**, 9, pp. 4606–4614, 2103.
32. Nguyen, D. M., Lee, D. & Rho, J. Control of light absorbance using plasmonic grating based perfect absorber at visible and near-infrared wavelengths. *Sci. Rep.* **7** (1), 2611 (2017).
33. Nayani, P. & Ra'Di, Y. Overcoming the Upper bound on the bandwidth-to-thickness ratio of ultrathin absorbers, 2023 Seventeenth International Congress on Artificial Materials for Novel Wave Phenomena (Metamaterials), vol. 1, no. 1, pp. X-244, (2023).

Acknowledgements

This work was supported in part by the AME Programmatic Grant, Singapore, under Grant A18A7b0058. The authors also acknowledge the support from the National Research Foundation of Singapore, through the National Semiconductor Translation and Innovation Centre (NSTIC). Z.W. thanks the Straetz International Undergraduate Research Scholars Program, from UChicago College Center for Research and Fellowships (CCRF), for supporting his stay in Singapore.

Author contributions

S.L. and Z.W. share equal contributions. Z.W. performed Lumerical FDTD simulations, S.L. performed RETICOLO RCWA simulations and near-field modelling. S.L. and E.L. prepared the manuscript. E.L. and R.P.-D. supervised the work.

Declarations

Competing interests

The authors declare no competing interests.

Additional information

Supplementary Information The online version contains supplementary material available at https://doi.org/10.1038/s41598-024-74796-5.

Correspondence and requests for materials should be addressed to E.L. or R.P.-D.